CLOUD BASE HEIGHT AND OPTICAL THICKNESS RETRIEVALS USING AVIRIS DATA

T. A. Berendes, R. E. Feind, K.-S. Kuo and R. M. Welch

Institute of Atmospheric Sciences
South Dakota School of Mines and Technology
Rapid City, South Dakota

Abstract. In this preliminary study, a 3-band ratioing technique (Gao and Goetz, 1990a) is applied to high spectral and spatial resolution AVIRIS imagery as a front-end process for the estimation of cloud base height and optical thickness. Spatial averaging is also applied to the AVIRIS imagery to investigate the effect of low spatial resolution data in the estimation of the same cloud properties.

I. INTRODUCTION

Understanding the role of clouds in the Earth's radiation budget is one of the highest priority science objectives in the EOS (Earth Observing System) program. In order to fully understand the formation and feedback processes of clouds, an accurate measurement of their properties is necessary. Remotely sensed data by satellites is an important source of information for monitoring clouds globally. Therefore, development of algorithms for the retrieval of cloud properties from satellite based instruments is paramount.

The presence of clouds makes it difficult to accurately model the surface energy budget. An uncertainty in cloud base height of 100 mb (~ 1 km) at the 650 mb (~ 4 km) level leads to an error of 5 W/m^2 in surface flux (Gupta, 1989). The effect of clouds on surface fluxes decreases as cloud base height and relative humidity increase. An accurate method for estimating cloud base height will aid in the modeling of the earth's radiation budget.

The transmission, reflection, and absorption of radiation in a cloudy atmosphere is influenced, in part, by the cloud optical thickness. Therefore the variations of cloud optical thickness will pose a significant impact upon earth radiative energy budget. Accurate retrieval of optical thickness is needed to make a reasonable assessment of the earth's energy budget. This study investigates the effect of spatial resolution upon the retrieval of optical thickness.

Two scenes acquired by the AVIRIS instrument over the Belize, Central America area are used for analysis in this preliminary study. Figure 1 shows an example of one of the AVIRIS scenes. This scene is a 5-channel average for the wavelengths centered at 1.04 μm. The clouds present in this scene are fair weather cumulus. Spatially averaged versions of both scenes are also generated for the analysis so that the type of results expected from low spatial resolution instruments can be assessed.

This paper is divided into three primary sections. Section II discusses the application of a 3-band ratioing technique. In Section III, a recently developed technique for cloud base height estimation is described, and results at various simulated spatial resolution are obtained. Section IV discusses the methodology used for retrieving the cloud optical thickness by way of the Discrete Ordinate radiative transfer model. Results at various simulated spatial resolutions are presented.

II. 3-BAND RATIOING AND CLOUD IDENTIFICATION

A. Gao and Goetz Technique

The identification of clouds in remote sensing imagery is the first major step in determining cloud properties (e.g., optical thickness, particle size, etc.). Each image pixel must be classsified as either cloud or non-cloud. Cloud pixels are used to determine cloud properties, and non-cloud pixels are considered to be part of the background and are therefore ignored. Most existing cloud identification algorithms rely on the selection of a threshold. The choice of the threshold can be somewhat subjective. Therefore, the results of any type of cloud property analysis can be highly variable dependent on the type of cloud identification algorithm used.

When high spectral resolution data is available, like that available from AVIRIS, identification of clouds can be achieved with greater confidence. Gao and Goetz (1990a) developed a technique that takes advantage of this high spectral resolution imagery, and greatly facilitates the ability to distinguish between cloud and background pixels. First, a 5-channel averaged radiance is computed for each pixel over the water vapor absorption channels centered at 0.94 and 1.04 μm, and the water vapor window channel centered at 1.04 μm. The 5-channel averaging filters out some of the noise present in the single channel imagery while still retaining sufficient spectral resolution for the technique to work. Next, the ratio of the sum of the radiance from the two water vapor channels to twice the radiance of the window channel, is computed, i.e.,

$$BR = (rad(.94) + rad(1.14))/(2 * rad(1.04)).$$

(This process will be referred to as 3-band ratioing and the ratio obtained as 3-band ratio, hereinafter.) The 3-band ratio values typically range from 0 to 2 and, therefore, are scaled from 0 to 255 for display purposes.

In the 3-band ratioed imagery, the background (when it is land) is somewhat homogenized, while the clouds retain their features (see Gao and Goetz, 1990a, for examples). The effect can be explained by the fact that most soil ingredients have a linear spectral response over the 0.94 to 1.14 μm wavelength region (Gao and Goetz, 1990b), whereas clouds have a nonlinear response. However, over uneven terrain, a brightness gradient will appear in the background of the ratioed image, as higher terrain results in shorter water absorption paths, hence less water absorption and larger ratios. This effect makes cloud identification with this technique more difficult and can result in false classification of cloud pixels.

An example of the effect of 3-band ratioing can be seen in Fig. 2 and Fig. 3 in the lower right quadrant (annotated as BR). The background

appears to become somewhat homogeneous; however, salt and pepper type noise appears in the regions corresponding to cloud shadows. This is caused by the fact that, over areas containing cloud shadows, the denominator of the ratio becomes very small and results in relatively large ratio values. Past experience has revealed that the same effect is manifested over water areas. Therefore, it is necessary to apply thresholds to the 3-band ratioed image to separate cloud pixels from background pixels.

B. Thresholding

Identification of clouds in the 3-band ratioed image is based on two thresholds, both derived from the histograms of the three 5-channel averaged images centered at 0.94, 1.04, and 1.14 μm. The histograms for these three images for one of the scenes processed for this paper appears in Fig. 4. These histograms can be viewed as the composite of three classes of pixels -- shadows cast by clouds, background features, and clouds. In each of the three histograms, two distinctive local maxima can be observed. The first (from the left) corresponds to the distribution of cloud shadow pixels, and the second to the distribution of the background pixels. The tail that extends to the right corresponds to the distribution of the cloud pixels (which does not exhibit an obvious peak).

The local minimum for the 0.94 μm image, (that occurs between the local maxima for cloud shadow and background) is used as the first threshold. For example, in Fig. 4, a value of 275 is selected for the threshold and is annotated as .94 (shadows). All pixels in the 3-band ratioed image are set to the minimum ratio (effectively zero) for all corresponding pixels in the 0.94 μm image with gray levels below the aforementioned local minimum. This threshold effectively filters away the salt and pepper noise caused by the cloud shadows and/or water.

The second threshold is based on the location of the discernible knee in each of the three histograms that occurs to the right of the local maximum for the background. For example, the location of the knee points in Fig. 4 are 450, 1750, and 220, and are annotated as .94 (backgrd), 1.04 (backgrd), and 1.14 (backgrd), respectively. These three points are then applied in the 3-band ratio relation above and the resulting value is used as the second threshold. Any pixel value in the 3-band ratioed image less than the second threshold is also set to the minimum ratioed value. Any other pixel that is not set to the minimum ratioed value then corresponds to cloud pixels.

Results for the 3-band ratioed images, using the above described thresholding, appear in Figs. 5 and 6 in the lower right quadrant (annotated as BR). The process has the effect of converting the background to black while retaining the cloud features.

The resulting ratioed image can then be applied as a mask to other channels for cloud identification (as is done in a subsequent section for the determination of cloud edges in a cloud base height algorithm and of optical thickness).

The above described process for selecting the second threshold was arrived at empirically and is not technically satisfying. The "knee points" were selected intuitively as it seems to be a reasonable demarcation between

the distributions for background and cloud pixels. Investigation is currently being conducted to develop a more technically sound approach for selecting an optimum decision point between the background and cloud pixels in each of the three histograms. Then the process can be automated so that manual selection of those points is not required.

C. Alternative 3-Band Ratioing Techniques

Two other band ratio relationships are implemented and preliminary results are compared with those obtained above. (They are referred to as BR2 and BR3, to distinguish them from the ratio described above which will be referred to as BR1.) The alternative 3-band ratios are:

$$BR2 = (2 * rad(.94))/(rad(.84) + rad(1.04))$$

$$BR3 = (2 * rad(1.14))/(rad(1.04) + rad(1.24))$$

These ratios attempt to take advantage of the same response characteristics of soil constituents and clouds in various water vapor absorption and window bands.

In Figs. 7 through 10 appear the results for two scenes in which the three 3-band ratioing techniques are applied. As a reference, in the upper left quadrant is the image from the 5-channel averaged image centered at 1.04 μm. For both figures, the results from BR1, BR2, and BR3 appear in the upper right, lower left, and lower right quadrants, respectively. In Figs. 7 and 8 are the results before the two thresholds are applied, and in Fig. 9 and 10 are the results after the two thresholds are applied. The method for selecting the two thresholds in BR2 and BR3 is the same as in BR1 with the exception that, in BR3, the histogram for the image centered at 1.14 μm is used for selecting the cloud shadow threshold.

It appears that similar results are obtained using BR1 and BR2; however, BR3 appears to provide much poorer performance. It is not yet known whether another threshold selection for BR3 would provide improved performance, or if falsely classified cloud pixels in the background area have the same gray level values as correctly classified cloud pixels. Further investigation is required in this area.

On close inspection, some noise can be observed in the thresholded results for BR1 and BR2. Although not used here, application of a median filter is effective in removing the noise with minimal loss of cloud edge pixels.

III. CLOUD BASE HEIGHT ESTIMATION

A semi-automated technique has been developed to estimate cloud base height using AVIRIS data. The algorithm consists of the following major steps:

A. Preprocessing

B. Pattern Matching

C. Cloud Base Height Estimation

A. Preprocessing

The goal of preprocessing is to reduce the image to cloud and shadow edge elements. This step employs several image processing techniques. First, a median filter is applied to the image to eliminate noise. The median filter was chosen because it is a very effective noise removal technique which also preserves the edge transitions in the image.

The image is reduced to its edge elements by a Laplacian of Gaussian filter (Huertas and Medioni, 1986). The Gaussian function has the following form:

$$G(x,y) = \frac{1}{2\pi\sigma^2} \exp \frac{-(x^2 + y^2)}{2\sigma^2} \quad ,$$

where σ is the standard deviation; x and y are horizontal and vertical offsets from a pixel of interest.

The Laplacian of Gaussian operation is performed by taking the Laplacian of the Gaussian function and convolving the result with the median filtered image, f(x,y). This results in a binary image composed entirely of pixels which correspond to the locations of edge transitions in the median filtered image. This edgemap, $f_e(x,y)$ is obtained as follows:

$$fe(x,y) = \nabla^2 G(x,y) * f(x,y) \quad .$$

The Laplacian of Gaussian filter reduces the image to 1 pixel wide lines. Figure 11A shows the image from Fig. 1 after the Laplacian of Gaussian filter has been applied. At this point, the image contains a large number of edges which correspond to legitimate edge transitions, but are not of interest to this study. Only cloud and shadow edges are useful for cloud base height estimation. All other edges should be eliminated.

It is difficult to visually determine which edge pixels correspond to cloud or shadow edges in Fig. 11A. A technique which we call max/min thresholding (Berendes et al., 1991) is applied to eliminate extraneous edges and classify remaining ones as either cloud or shadow. Max/min thresholding constructs a localized histogram of gray level values surrounding each edge pixel in the median filtered image. The histograms typically have three peaks which correspond to cloud, background, and shadow pixels. If water is present, an additional peak will occur at a gray level below the shadow peak. The peaks of the histogram are found, and cloud and shadow thresholds are determined using a weighted averaging technique. The cloud and shadow thresholds are used to determine the type of transition which is occurring at an edge pixel. Since we are only interested in cloud and shadow edges, only the following transitions are of interest:

Cloud ⟷ Shadow

Cloud ⟷ Background

Background ⟷ Shadow

By applying the cloud and shadow thresholds, edge pixels which do not correspond to one of the above transitions are eliminated, and the remaining edge pixels are classified as either cloud or shadow.

The band ratioing technique described in the previous section has been used to eliminate the background and leave only the clouds in the image. This technique simplifies the basic algorithm since a simple threshold can be applied to the ratioed image to set clouds to one gray level. This creates a binary image from which edges can easily be determined by means of a Roberts operator. Therefore, the max/min thresholding is not used to determine cloud edges. Figure 11B shows the cloud edges of Fig. 1.

Since shadows are eliminated in the band ratioed image, max/min thresholding must still be used to find the shadow edges. The 1.04 μm band is used to find shadow edges because it provides good contrast between the shadows and the background. The max/min thresholding technique is used in this case to find only shadow edges and eliminate all others. Figure 11C shows the shadow edges extracted from Fig. 11A.

After cloud and shadow edges are found, they are combined together in one image. Figure 11D shows Fig. 11B combined with Fig. 11C. The brighter pixels are cloud edges, and the darker ones are shadow edges. Pattern matching can now be performed on this image.

B. Pattern Matching

The Generalized Hough Transform (Ballard, 1981) is a pattern matching technique which is capable of matching arbitrary patterns. In this case, cloud edges are matched with their corresponding shadow edges. The Generalized Hough Transform cloud base height algorithm can be described by the following steps:

1) Parameterize desired cloud edge with respect to an arbitrary fixed reference point near the cloud edge;
2) Within a search area, search for shadow edge which best matches the cloud edge.
3) Find the shadow edge which best matches the cloud edge and calculate the location of a new reference point with respect to the found shadow edge.

C. Cloud Base Height Estimation

Once the location of the new reference point has been determined, the separation distance between the two reference points can be used to determine the cloud base height using the following equation:

$$h = d/\tan \theta_0$$

where d is the separation distance, θ_0 is the solar zenith angle.

Currently, cloud edges are selected manually. Selection of cloud edges for pattern matching is a critical part of the algorithm. In order

to minimize possible effects of cloud vertical development, cloud edges which are roughly parallel to the solar azimutal plane, and lie at a maximum distance from the center of the cloud are chosen for pattern matching. Figure 12A shows the edges which are chosen for an idealized cloud. Edges near points P or R are chosen for pattern matching. If an edge near point C is chosen, the error x in Fig. 12A and 12B will represent an elongation of the shadow due to vertical development. If a hemispherical shape is assumed, the corresponding error in cloud base height is given by b in Fig. 12C.

The viewing angle of the aircraft can also cause errors in cloud base height calculations. In Fig. 12B, if the aircraft is viewing at an angle θ from nadir, it will "see" under the cloud. This causes the perceived distance d between the cloud and shadow to be greater than the actual distance. The opposite situation occurs if the viewing angle is from the other direction. In either case, a correction must be made to account for off nadir viewing. If a correction is not made, errors in cloud base height of several hundred meters can occur if the cloud is located toward the right or left edge of the image. This error has been corrected for in the results.

The previous techniques have been applied to two AVIRIS scenes. The results can be seen in Figs. 13 and 14. The numbers indicate base heights in meters of individual clouds. The original reference point is represented as a black cross and the new reference point is a white cross. The images are of the 1.04 μm band. Most of the clouds in both images have a base height between 1 and 1.5 km.

The cloud base height algorithm has been applied successfully to LANDSAT and AVIRIS data. Both of these data types have high spatial resolution; 20 m for AVIRIS, 28.5 m for LANDSAT TM, and 57 m for LANDSAT MSS. Since some of the EOS instruments will have much lower resolution, we would like to determine how the algorithm will work at lower spatial resolutions. The heights of three clouds are shown in Fig. 15. Their heights are calculated based on the full resolution of the data. The cloud base height algorithm is also applied to a spatially averaged version of the image in Fig. 15. Figure 16 shows the heights of the same clouds in a spatially averaged version of the same image. The image has been spatially averaged to an effective pixel resolution of 120 m and shown here at the original size of the image. Notice that the cloud base heights in the averaged image are all higher than their counterparts at the original resolution.

A detailed study of the effects of degraded spatial resolution will be performed in the near future. However, in a preliminary investigation it is clear that spatial resolution has a very strong effect on both the performance of the cloud base height algorithm and the results obtained by the method. The method fails when a spatial resolution of 240 m/pixel is used. In this case, the resulting image is too small to work with effectively. Small clouds and shadows are averaged into the background. These difficulties make it nearly impossible to study the effects of spatial resolutions coarser than 240 m/pixel. Even at 120 m/pixel spatial resolution, many clouds that are used successfully at 20 m/pixel resolution are unusable or not visible.

IV. OPTICAL THICKNESS RETRIEVAL

A. Procedure

For contouring optical thicknesses of clouds in an image, we first assume a reasonable cloud droplet size distribution for the type of clouds under study. In this case, we have chosen the well known C1 distribution (Diermendjian, 1969) which is considered reasonable for fair weather cumulus -- the type of clouds analyzed in this study. The C1 distribution is a modified gamma distribution with the following form:

$$n(r) = a\, r^{\alpha} \exp(-\, br^{\gamma}) \quad ,$$

where n(r) is the number concentration at radius r (in μm). The values of the parameters are a = 2.373, α = 6.0, b = 1.5, and γ = 1.0. This choice of parameters yields an effective radius of 6 μm.

We then run a Mie scattering calculation at 0.742 μm on this C1 cloud droplet size distribution to get the Legendre polynomial expansion for the scattering phase function. The 0.742 μm channel is chosen because, at this wavelength, reflectance becomes insensitive to cloud droplet size (effective radius) and is sufficiently long to avoid Rayleigh scattering (Nakajima and King, 1990). In turn, with other specification parameters, the Legendre polynomial expansion of the phase function is input to the Discrete Ordinate radiative transfer model which assumes plane-parallelism on the media. The other parameters include the solar zenith angle, background albedo, and optical thickness.

The solar zenith angle is calculated using local latitude, longitude, and time data from the navigation file associated with the image. The background albedo is assumed to be the value where the second local maximum occurs in the histogram for the 0.742 μm image (Wielicki and Welch, 1986). For example, for scene B, the background albedo is taken to be 22% (see Fig. 17). The set of optical thicknesses -- 0, 1, 2, 4, 8, 10, 12, 14, 16, 18, 20, 24, 28, 32, 40, 48 -- are chosen for calculation. For each optical thickness, the radiative transfer model returns the nadir reflectance that would be observed and is used for the optical thickness color-slicing of the 0.742 μm image.

B. Application of 3-Band Ratioing in the Determination of Cloud Optical Thickness

The 3-band ratioed images derived above are applied to the image corresponding to the 0.74 μm channel. All pixels in the 0.742 μm image are set to zero for any corresponding pixel in the band ratioed image with a minimum 3-band ratioed value. All other pixels (cloud pixels) retain their original value. In this way, all of the background is masked out, leaving only cloud pixels. Figure 18 shows a 0.742 μm image after being masked. Based on results from the Discrete Ordinate radiative transfer model, the cloud pixels are color sliced into 16 discrete optical thickness contours. Results for the two scenes studied appear in the upper left quadrants of Figs. 19 and 20 [see slides 20 and 21].

C. Reduced Spatial Resolution and Optical Thickness

In an attempt to better understand the relationship between optical thickness results obtained from high spatial resolution imagery (such as AVIRIS) and low spatial resolution imagery (such as MODIS), cloud optical thickness is recomputed for each of the two scenes for three additional cases. In the three cases, the high spatial resolution AVIRIS imagery is spatially averaged over 3 x 3, 6 x 6, and 12 x 12 pixel areas to simulate the imagery obtained from instruments with spatial resolutions of 60 m, 120 m, and 240 m (the highest spatial resolution available from MODIS), respectively. The results for optical thickness obtained from these spatially averaged images appear in Figs. 19 and 20, in the upper right, lower left, and lower right quadrants for 60 m, 120 m, and 240 m imagery, respectively.

A couple of observations can be made through inspection of these images. One is that the optical thickness appears to decrease as spatial resolution decreases. Optically thicker areas become thinner as they are averaged with neighboring thinner areas (such as background). Another is that the cellular structure of the clouds becomes obscured as spatial resolution is decreased.

The average optical thicknesses for each of the two scenes and for each of the spatially degraded images are calculated and are summarized below:

	Spatial Resolution	Average Optical Thickness
Scene A	20 m	6.12
	60 m	4.14
	120 m	4.13
	240 m	3.92
	480 m	3.35
	960 m	2.87
Scene B	20 m	6.32
	60 m	5.47
	120 m	5.45
	240 m	5.38
	480 m	5.05
	960 m	4.36

These results seem to support the above observation that, as spatial resolution is increased, so does optical thickness. However, these results are not sufficiently extensive to make that conclusion. Analysis of additional scenes is currently in progress to investigate this phenomena and will be reported on at a future date.

V. CONCLUSIONS

Three-band ratioing, followed by thresholding, appears to provide a reliable technique for identifying cloud pixels in high spectral resolution imagery. The ratioed image can be used as a mask to eliminate the effect of the background in cloud property retrievals.

The Hough Transform cloud base height algorithm has been successfully applied to AVIRIS data. The addition of the band ratioing technique simplifies the extraction of cloud edges from the scenes.

In this preliminary investigation, it has been observed that spatial resolution has a profound effect upon the performance and results of the cloud base height algorithm. At spatial resolutions less than 100 m/pixel, the cloud base height algorithm is more likely to fail to match cloud and shadow edges. The cloud base heights obtained at 120 m/pixel resolution are substantially higher than those obtained at 20 m/pixel resolution. It seems doubtful that the cloud base height algorithm could be applied successfully to data with a spatial resolution coarser than 150 m/pixel.

When simulating low spatial resolution, by spatially averaging high spatial resolution imagery, the overall optical thickness of clouds in a scene appears to decrease. This is evidenced by both the optical thickness contours and the values obtained for average optical thickness.

VI. Future Work

Only two scenes were analyzed in this study. The above described procedures need to be tested on many more. For example, they will be applied to a wider variety of scene types, including those that contain uneven terrain, water, snow, and other cloud types. The following will be investigated over this larger data set:

- Improved methods for selecting thresholds, that can be implemented in an autonomous environment.
- The effect of spatial resolution in cloud property retrievals, and, in particular, cloud base height, optical thickness, particle size, cloud size, and effective radius.
- The effect of various cloud droplet size distributions in the calculation of optical thickness.

References

Ballard, D. H., 1981: Generalizing the Hough Transform to detect arbitrary shapes. Pattern Recognition, 13, 111-122.

Berendes, T., S. K. Sengupta, R. M. Welch, B. A. Wielicki, and M. Navar, 1991: Cumulus cloud base height estimation from high spatial resolution Landsat data: A Hough transform approach. [Submitted to IEEE Trans. Geosci. Remote Sens.]

Diermendjian, D., 1969: Electromagnetic scattering on spherical polydispersions. American Elsevier Publishing Company, New York. 290 pp.

Gao, B-C., and A. F. H. Goetz, 1990a: Determination of cloud area from AVIRIS data. Proceedings 2nd AVIRIS Workshop. JPL Publication 90-54.

_____, and _____, 1990b: Column atmospheric water vapor and vegetation liquid water retrievals from airborne imaging spectrometer data. J. Geophys. Res., 90, D4, 3549-3564.

Gupta, S. K., 1989: A parameterization for longwave surface radiation from sun-synchronous satellite data. J. Climate, 2, 305-320.

Huertas, A., and G. Medioni, 1986: Detection of intensity changes with subpixel accuracy using Laplacian-Gaussian masks. IEEE Trans. Pattern Anal. Mach. Intell., 8, 651-664.

Nakajima, N., and M. D. King, 1990: Determination of the optical thickness and effective particle radius of clouds from reflected solar radiation measurements. Part 1: Theory. J. Atmos. Sci., 47, 1878-1893.

Wielicki, B. A., and R. M. Welch, 1986: Cumulus cloud properties derived using Landsat satellite data. J. Climate Appl. Meteor., 25, 261-276.

Acknowledgments

This work was conducted jointly under National Aeronautics and Space Administration (NASA) Contracts NAS5-30768 and NAS5-30958 and Jet Propulsion Laboratory Contract 000573907. Thanks are extended to Joie Robinson for typing this manuscript.

Fig. 1: 5-channel averaged radiance image for Scene A at 1.04 μm.

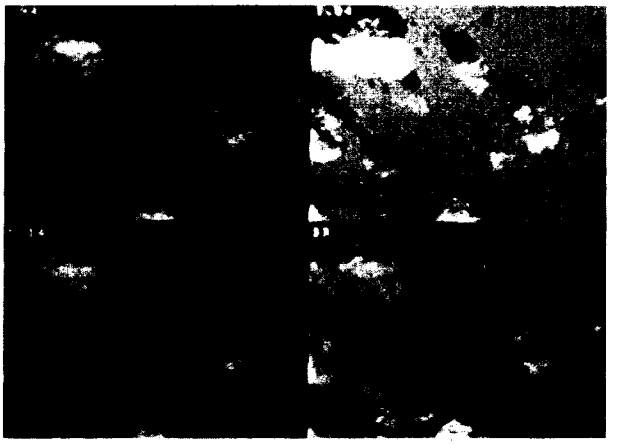

Fig. 2: 5-channel averaged radiance image for Scene A at 0.94 μm (upper left), 1.04 μm (upper right), 1.14 μm (lower left), and 3-band ratioed image (lower right).

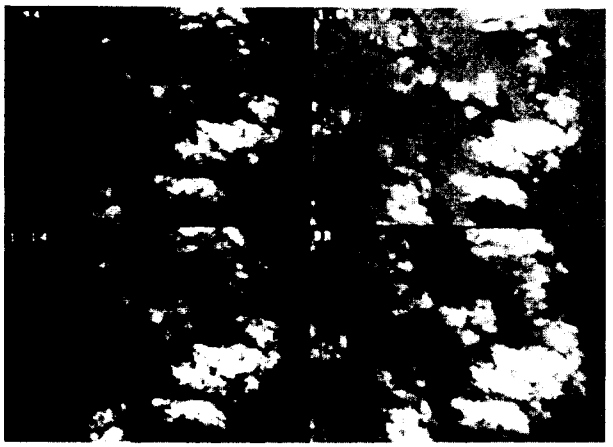

Fig. 3: Same as Fig. 2 for Scene B.

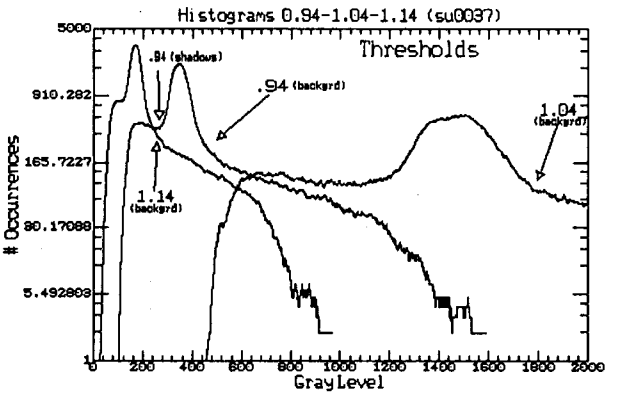

Fig. 4: Histograms for 5-channel averaged radiance images at 0.94, 1.04, and 1.14 μm for Scene B.

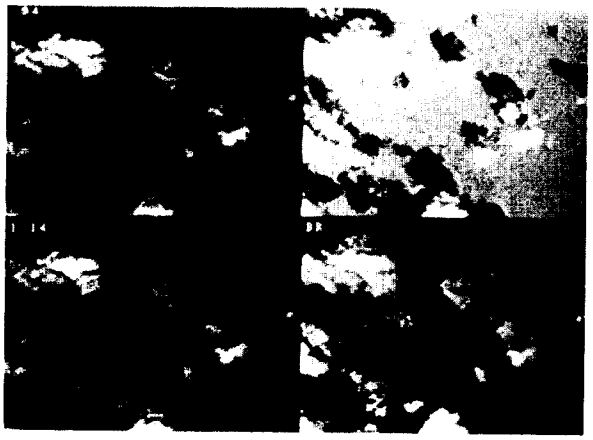

Fig. 5: 5-channel averaged radiance image for Scene A at 0.94 μm (upper left), 1.04 μm (upper right), 1.14 μm (lower left), and 3-band ratioed image with thresholding (lower right).

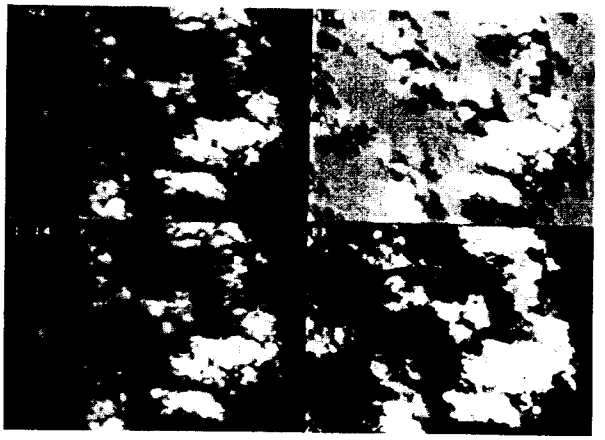

Fig. 6: Same as Fig. 5 for Scene B.

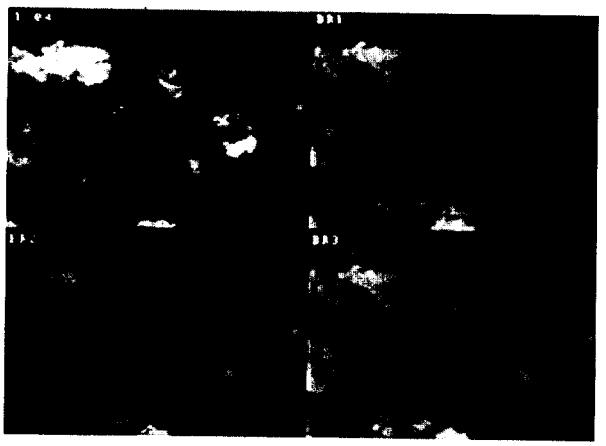

Fig. 7. 5-channel averaged radiance image for Scene A at 1.04 μm (upper left); 3-band ratioed image without thresholding using Gao and Goetz technique (upper right); alternative 3-band ratioed images without thresholding (lower left and lower right; see text for details).

Fig. 8: Same as Fig. 7 for Scene B.

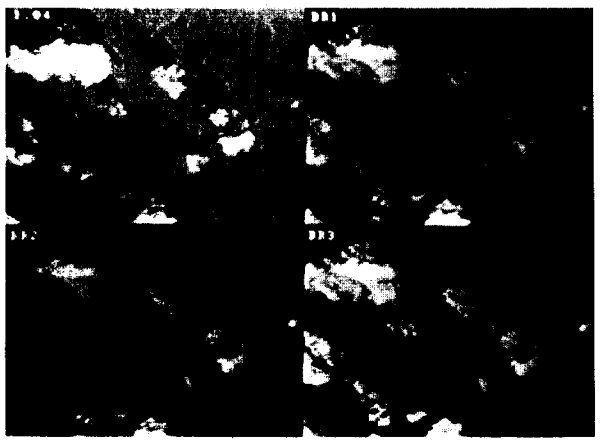

Fig. 9: 5-channel averaged radiance image for Scene A at 1.04 μm (upper left); 3-band ratioed image without thresholding using Gao and Goetz technique (upper right); alternative 3-band ratioed images with thresholding (lower left and lower right; see text for details).

Fig. 10: Same as Fig. 9 for Scene B.

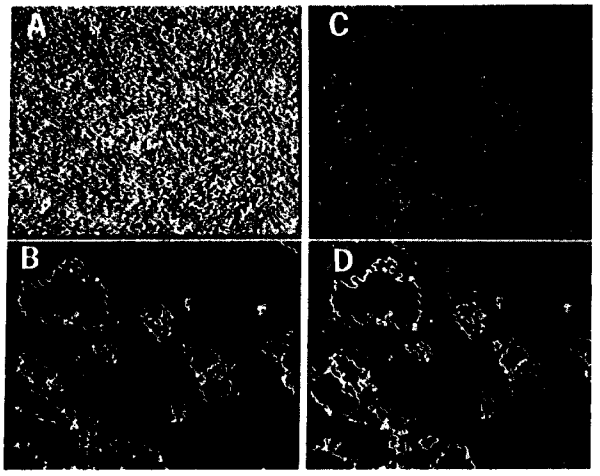

Fig. 11: A) Laplacian of Gaussian image of Fig. 1; B) cloud edges extracted from B-band ratioed image; C) shadow edges extracted from 1.04 μm band using max/min thresholding; and D) combination of Figs. B and C.

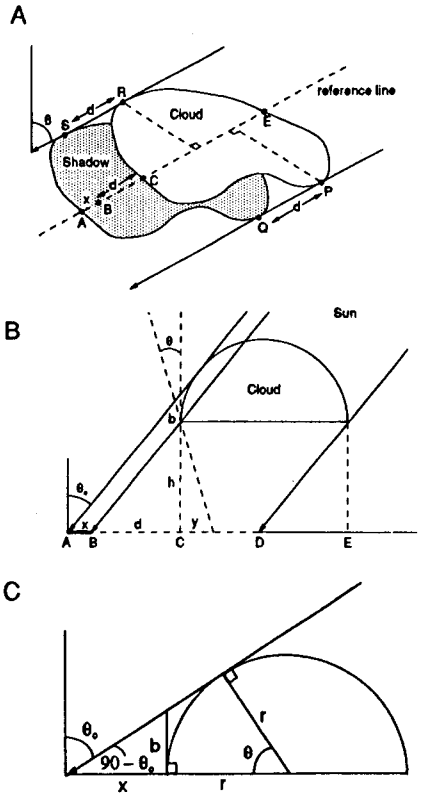

Fig. 12: A) An idealized cloud and its shadow; B) vertical cross section of Fig. A. Potential error in horizontal separation distance is given by x; and C) resulting error in cloud base height is b.

Fig. 13: Results of cloud base height estimation for Scene A. Black crosses are the original reference points. White crosses are the new reference points.

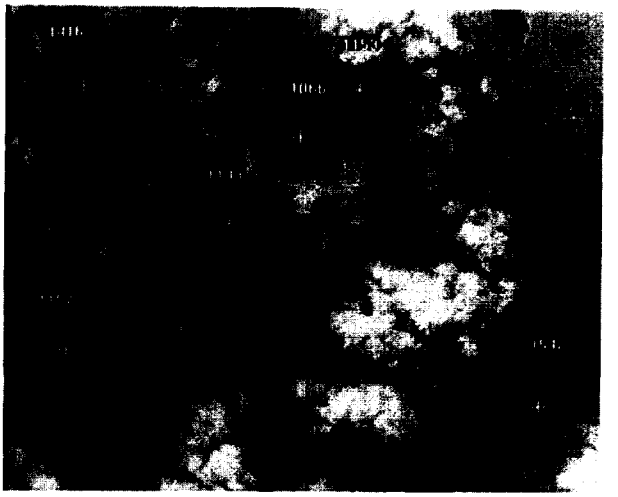

Fig. 14: Results of cloud base height estimation for Scene B. Black crosses are the original reference points. White crosses are the new reference points.

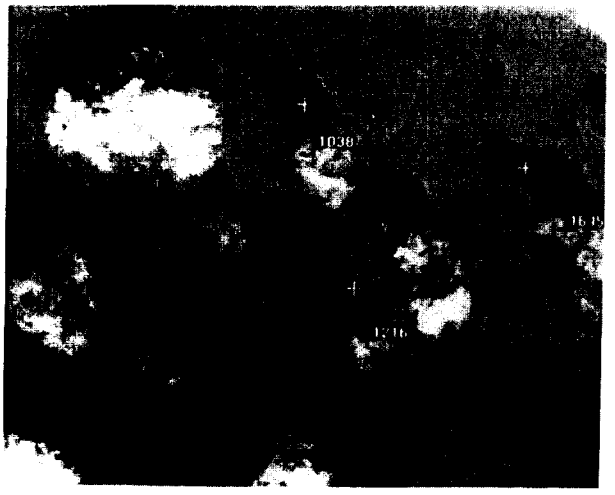

Fig. 15: Results of three selected clouds in Scene A at 20 m/pixel spatial resolution.

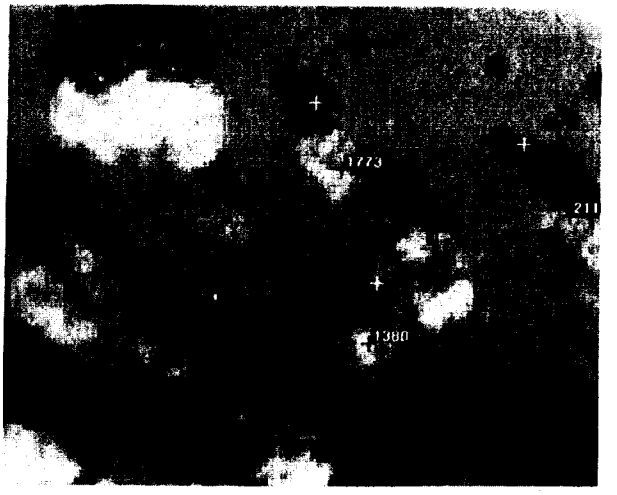

Fig. 16: Results of the same three clouds chosen in Fig. 15 at 120 m/pixel spatial resolution.

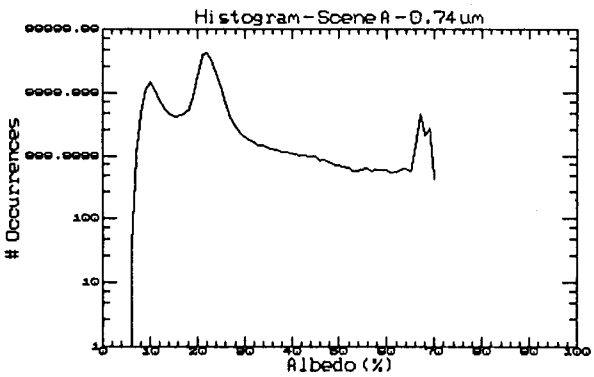

Fig. 17: Histogram of albedo for 0.742 μm image.

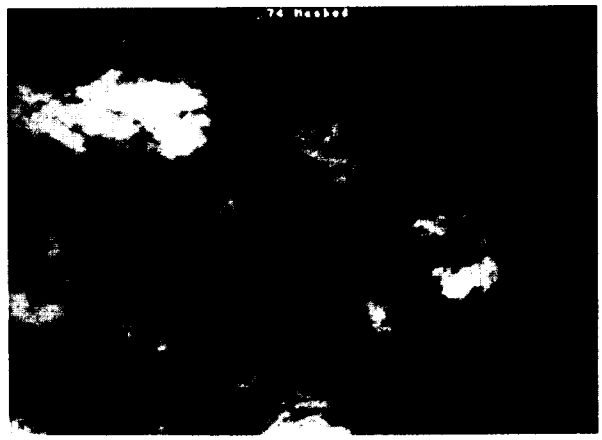

Fig. 18. A 0.742 μm image with background masked by 3-band ratioed image.

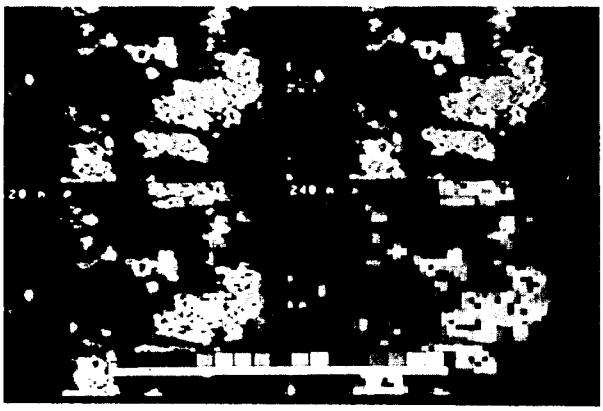

Fig. 19: Optical thickness contours for Scene A at 20 m, 60 m, 120 m, and 240 m spatial resolution: (see slide 20).

Fig. 20: Same as Fig. 19 for Scene B: (see slide 21).